Geophysical Research Letters

RESEARCH LETTER
10.1029/2025GL120303

Salt Precipitation-Driven Rock Failure Mode Transition During Geological CO_2 Sequestration

Senyou An[1], Junjie Ju[1], Ji Kong[1], Ying Teng[1], Lifei Yan[2], Pengfei Wang[3], Jianbo Zhu[1], and Heping Xie[1]

[1]State Key Laboratory of Intelligent Construction and Healthy Operation and Maintenance of Deep Underground Engineering, College of Civil and Transportation Engineering, Shenzhen University, Shenzhen, China, [2]Faculty of Civil Engineering and Geosciences, Delft University of Technology, Delft, The Netherlands, [3]Shenzhen Key Laboratory of Natural Gas Hydrates, Advanced Institute for Ocean Research, Southern University of Science and Technology, Shenzhen, China

Key Points:

- Salt precipitation drives a transition in rock failure mode from shear-to tensile-dominated behavior
- Multiscale characterization reveals crystallization-induced initiation and propagation of microcracks
- Mechanical properties degrade systematically after precipitation, with reduced strength and stiffness

Supporting Information:

Supporting Information may be found in the online version of this article.

Correspondence to:

S. An,
senyouan@szu.edu.cn

Citation:

An, S., Ju, J., Kong, J., Teng, Y., Yan, L., Wang, P., et al. (2026). Salt precipitation-driven rock failure mode transition during geological CO_2 sequestration. *Geophysical Research Letters*, *53*, e2025GL120303. https://doi.org/10.1029/2025GL120303

Received 4 NOV 2025
Accepted 25 JAN 2026

Abstract Salt precipitation has emerged as a critical factor affecting injectivity, reservoir stability, and the potential to trigger near-wellbore microseismic activity during geological CO_2 sequestration. While previous studies have primarily focused on the brine acidification induced by CO_2 injection, triggering geochemical reactions in carbonate rocks and leading to mechanical degradation, the mechanical behavior associated with salt precipitation in drying zones, particularly the failure mechanisms, remains poorly understood. In this work, we designed a reservoir-condition displacement system to mimic near-wellbore drying process and further investigated the rock failure modes due to salt precipitation in red sandstone samples. Our study demonstrates that, despite the densification of the pore structure due to salt precipitation, the overall mechanical performance of the rock undergoes significant deterioration. More importantly, for the first time, we observe a distinct transition of failure mode from shear-to tensile-dominated under uniaxial compression. Microstructural analysis further shows that the growth of polycrystalline and bulk crystals induces microcrack initiation and propagation, with the failure mechanism of rocks subjected to salt precipitation primarily characterized by intercrystalline damage at weak bonding interfaces under external loading.

Plain Language Summary Geological sequestration of CO_2 has emerged as a promising and viable strategy to mitigate climate change by injecting supercritical CO_2 ($scCO_2$) into deep subsurface formations for long-term containment. This process can induce salt precipitation, a phenomenon where dissolved salts crystallize out of pore brine. Such precipitation poses significant challenges, including pore blockage, reduced rock strength, and a potential contribution to microseismicity that may compromise reservoir stability. In this study, the effects of salt precipitation on the microstructure and failure characteristics of reservoir rocks were experimentally investigated under reservoir-representative conditions. Results indicate that while salt crystallization densifies the rock's pore structure, it paradoxically undermines the overall mechanical integrity. Specifically, the load-bearing capacity is significantly reduced, making the rock increasingly prone to tensile failure as opposed to shear failure under compressive stress. Given that fluid injection most commonly induces shear failure, particularly in the presence of pre-existing faults, a shift toward tensile-dominated failure makes reservoir damage more complex. Moreover, tensile failure promotes fracture opening and propagation, thereby increasing uncertainty in CO_2 migration prediction and monitoring. This transition in failure mode is attributed to weak interfacial bonding between the salt crystals and the rock matrix, along with an increased development of microcracks. These findings provide critical insights into the stability of geological reservoirs during CO_2 sequestration and establish a scientific basis for investigating the mechanisms of injection-induced microseismicity.

1. Introduction

As the world grapples with the challenges of climate change, reducing atmospheric CO_2 concentrations has become a critical scientific imperative (An et al., 2021; Chai, Liu, Wang, et al., 2022; Krevor et al., 2023; Wang et al., 2023). Geological CO_2 sequestration (GCS) emerges as a vital strategy for mitigating climate change, with a focus on identifying ideal storage reservoirs that balance large storage capacity, efficient injectivity, and long-term structural integrity (Celia et al., 2015; De Silva et al., 2015; Gandomkar et al., 2025; Li et al., 2023; Viswanathan et al., 2022). However, previous studies have highlighted the complexities of CO_2 injection, including

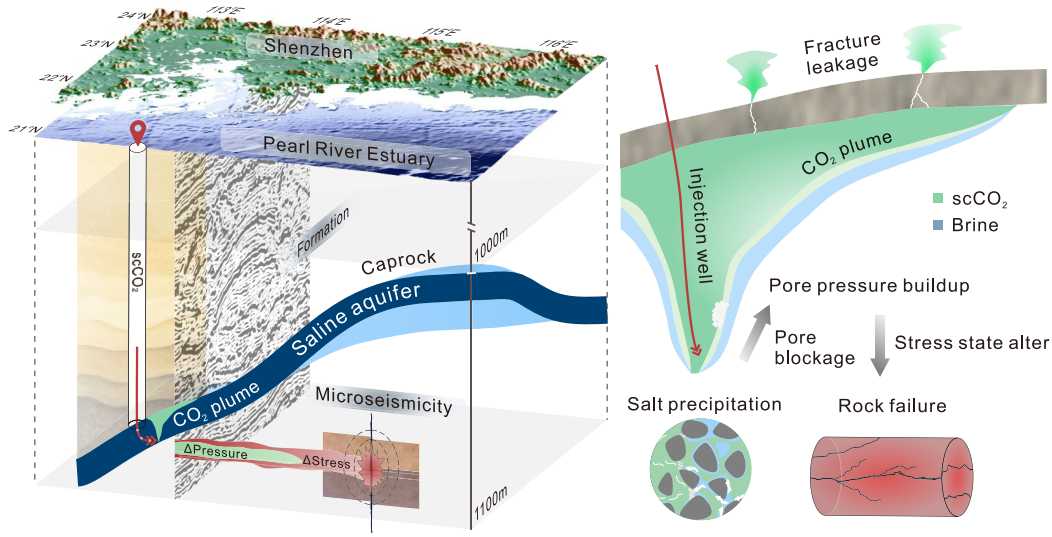

Figure 1. Schematic illustration of possible processes induced by $scCO_2$ injection in the Pearl River Estuary, including salt precipitation, pore blockage, pressure buildup, rock failure, and associated microseismicity.

salt precipitation in the near-wellbore region, which can lead to pore-scale blockage, increased injection pressure, and compromised injectivity (Ji et al., 2025; Sun et al., 2025). Moreover, this region, often identified as a hotspot for microseismic activity (Yu et al., 2023), may experience enhanced seismic responses resulting from pressure buildup associated with salt accumulation. Therefore, a comprehensive understanding of how salt precipitation affects the mechanical behavior and failure characteristics of reservoir rocks is essential for ensuring the stability and integrity of GCS systems.

Salt precipitation is a common geochemical phenomenon observed across various engineering fields, including soil salinization (Bergstad & Shokri, 2016; Hassani et al., 2024; Shokri et al., 2024), preservation of historical monuments (Espinosa-Marzal & Scherer, 2010; Scherer, 2004), and geochemical processes related to geological integrity (Jannesarahmadi et al., 2024; Wang et al., 2025). In deep geological environments, such as GCS sites, salt precipitation is particularly pronounced and complex near the injection wellbore. While CO_2 storage typically occurs in high-permeability reservoirs, field observations from the Ketzin site in Germany (Baumann et al., 2014) and the Snϕhvit project in Norway (Grude et al., 2014) have confirmed that salt precipitation can lead to complete pore clogging, thereby significantly impairing injectivity and increasing project costs. This phenomenon involves a series of interactions between water evaporation, solute transport, and capillary backflow, thereby amplifying the complexity of the injection system (An et al., 2020; Chen et al., 2024; Ji et al., 2025; Yan et al., 2025). Moreover, previous studies have demonstrated that elevated pore pressure can perturb the in situ stress field of the reservoir, rendering the rock mass more prone to failure. Once failure occurs, the elastic energy stored in the formation is released, triggering (micro)seismic events (Song et al., 2023; Vilarrasa et al., 2019). The pressure buildup induced by salt precipitation may therefore act as a potential factor contributing to the initiation of such microseismic activities, as illustrated in Figure 1. Furthermore, in recent years, physics-based microseismic prediction models have increasingly relied on a wide range of parameters, including the properties of reservoir rocks that have undergone coupled geophysical and geochemical interactions (e.g., salt precipitation) during CO_2 injection (Kivi et al., 2023, 2025).

The mechanical response of rocks during CO_2 injection can be investigated through coupled flow experiments and mechanical testing. These experiments yield valuable insights into the response mechanisms of the reservoir rock and provide an experimental basis for investigating the triggering mechanisms as well as the monitoring and assessment of microseismic events. Nevertheless, current research predominantly focuses on carbonate rocks (Li et al., 2022), emphasizing the chemical-hydraulic-mechanical (CHM) coupling effects induced by CO_2-acidified brine, which lowers brine pH and subsequently triggers mineral dissolution and precipitation reactions that reconstruct the pore-scale microstructure of the rock (Eberli et al., 2003; Eyitayo et al., 2025; Lyu et al., 2024). These microscale changes significantly impact hydrodynamic properties such as porosity and permeability (Alam

et al., 2014; Tao et al., 2023), which in turn influence the macroscopic mechanical response of the rock mass (Chai, Liu, Xue, et al., 2022; Hangx et al., 2013; Vialle & Vanorio, 2011; Xie et al., 2011). While the weakening effects of mineral dissolution and precipitation on rock structure and mechanical behavior have been widely emphasized, most GCS sites are predominantly composed of sandstone formations that remain comparatively underexplored. In particular, the geophysical and geochemical responses associated with evaporation-induced salt precipitation in dry zones are still rarely investigated.

This study identifies, for the first time, that salt precipitation drives a transition in rock failure from shear-to tensile-dominated modes. Through core-flooding experiments under dry-zone conditions and uniaxial compression tests, paired with a CO_2-deionized water displacement control to eliminate acidification effect, we isolate the role of salt crystallization in altering reservoir rock failure. Multiscale characterization and mechanical analysis provide new experimental evidence and theoretical insight into salt-induced damage and failure-mode transitions. These findings clarify the interplay among CO_2 injection, salt precipitation, and rock failure, with important implications for ensuring the long-term integrity of GCS and for advancing the understanding of the triggering mechanisms of microseismicity.

2. Materials and Methodologies

Homogeneous red sandstone, representative of typical GCS reservoirs, was used as experimental material. The cylindrical specimens (20 mm × 40 mm) mainly consisted of quartz and feldspar, as confirmed by X-ray diffraction and scanning electron microscopy coupled with energy-dispersive spectroscopy (SEM-EDS). These minerals exhibit low reactivity with CO_2 under reservoir conditions, allowing a clear distinction between salt precipitation and acid-induced effects. Mercury intrusion porosimetry and CT analyses indicated a relatively uniform and concentrated pore-size distribution, consistent with high-quality reservoir sandstone. Detailed mineralogical and pore-structure information is provided in Figure S1 in Supporting Information S1. To ensure accuracy and consistency, the rock specimens were ultrasonically cleaned, dried, and subjected to ultrasonic velocity measurements. Specimens with similar densities and wave velocities were selected for the experiments. A total of 18 red sandstone cores were selected and divided into three groups: untreated group (UT), deionized water displacement by $scCO_2$ group (DW, serving as a control to eliminate CO_2 acidification effects), and salt precipitation group (SP). Detailed sample information is provided in Table S1 in Supporting Information S1.

The displacement experiments were conducted at 9 MPa and 50°C to represent in situ reservoir conditions of the *X* offshore site in Pearl River Estuary (Sun et al., 2016; Zhou et al., 2011). The confining pressure was dynamically adjusted to track the pore pressure and maintained 3.5 MPa higher than the pore pressure throughout the experiments ($\Delta P = 3.5$ MPa). A 25 wt% NaCl solution was used as a reservoir brine. The detailed experimental procedures of the displacement experiments applied to all samples are provided in Section S3 in Supporting Information S1. After displacement, uniaxial compression tests were performed under displacement control at a rate of 0.3 mm/min using a Universal Testing Machine. A thin lubricant was applied to minimize end friction, and axial strain was continuously recorded using a linear variable differential transformer. Following the mechanical tests, microstructural and damage characteristics were analyzed through SEM, EDS, and CT, providing multi-scale insights into the structural changes induced by salt precipitation.

3. Results and Discussions

3.1. Effects of Salt Precipitation on Wave Velocity and Pore Structure

To investigate the evolution of rock failure modes induced by salt precipitation, elastic wave velocity was introduced in this study as a diagnostic parameter. As a sensitive indicator of internal structural changes, wave velocity is closely related to porosity, wave propagation pathways, and medium connectivity, and is widely used in non-destructive evaluation of rock physical properties and mechanical performance. In particular, wave velocity variation is strongly associated with the development of microcracks and the degree of structural integrity of the rock mass (Pellet & Fabre, 2007), providing valuable reference for subsequent analysis of mechanical response and failure characteristics. Figure 2a presents the test results of elastic wave velocities under different treatment conditions, with corresponding data provided in Table S2 in Supporting Information S1. The results indicate that, for the DW group samples, the P-wave and S-wave velocities showed a slight overall increase after treatment, though minor decreases were observed in a few samples. In contrast, the SP group samples exhibited a significant increase in elastic wave velocities. Specifically, the P-wave velocity

10.1029/2025GL120303

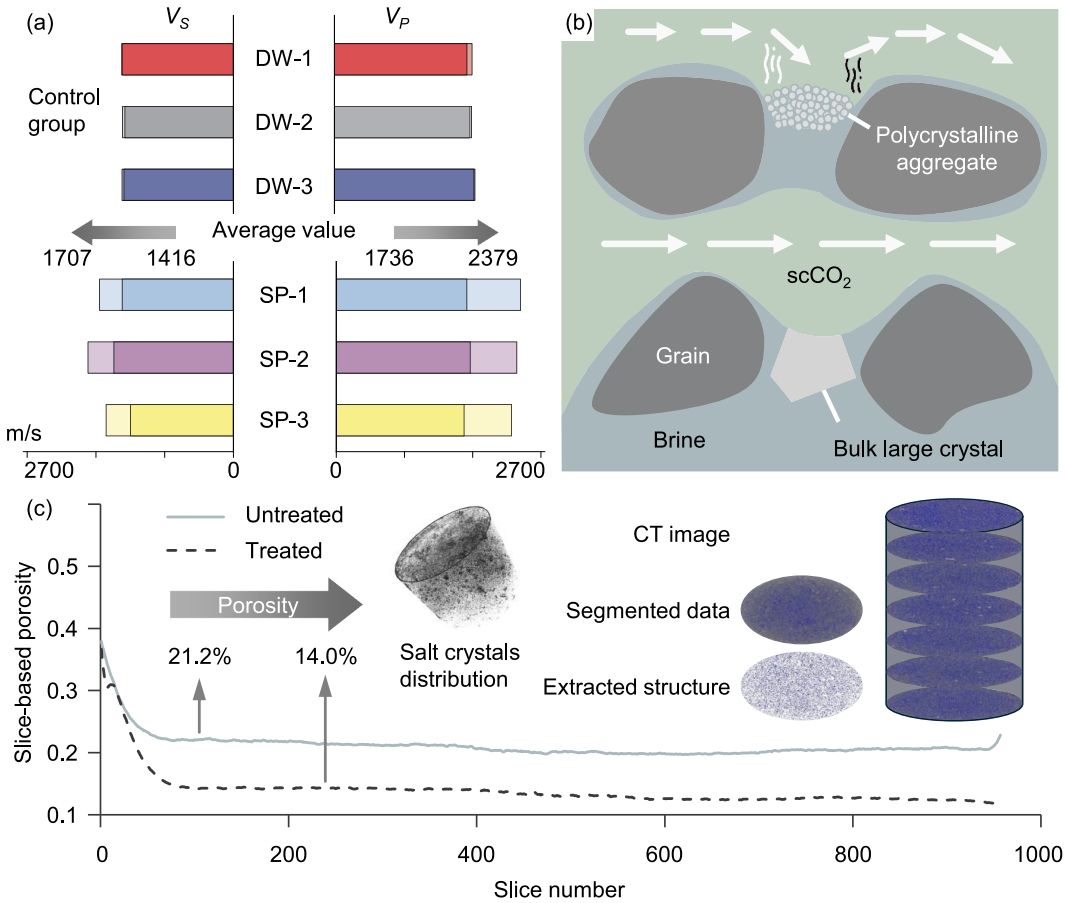

Figure 2. Effects of salt precipitation on wave velocity and pore structure in sandstone samples. (a) P- and S-wave velocity variations before and after experiments for the control (UT) and SP groups, showing significant increases in the SP group. (b) Schematic illustration showing two types of salt crystal morphologies, bulk large crystals and polycrystalline aggregates. White arrows indicate the $scCO_2$ flow direction. (c) CT-based analysis showing the CT processing workflow, the distribution of salt crystals concentrated within approximately 1.5 cm from the injection inlet after salt precipitation, and porosity reduction in this region, representing the general trend observed in most samples and consistent with prior studies.

increased from 1,736 m/s to 2,379 m/s, representing an average increase of 37.1%, while the S-wave velocity rose from 1,416 m/s to 1,707 m/s, corresponding to an average increase of 20.6%. These trends suggest that salt precipitation induced by CO_2 injection significantly improved the wave propagation characteristics by altering the rock's pore structure, making it the dominant factor contributing to the observed velocity increases.

The changes in pore structure during salt precipitation can be attributed to the nucleation and growth of salt crystals at the pore scale. Previous studies have shown that during $scCO_2$ injection, the displacement of brine mainly occurs through viscous flow and evaporation into the CO_2 stream, occurring at distinct timescales. Initially, the displacement is dominated by the two-phase viscous flow of $scCO_2$ and brine, rapidly removing most of the pore brine and establishing a residual brine saturation. Notably, the well-homogenized characteristics of the samples employed in this study result in relatively high residual brine saturation, attributed to the formation of CO_2 preferential flow pathways. The remaining brine exists primarily as thin films around grains, domes, pools, and liquid bridges. As dry $scCO_2$ with low water vapor pressure continues to be injected, the residual brine near the inlet begins to evaporate into the CO_2 stream. The evaporation front forms and advances along the injection direction. A brine saturation gradient is established, driving a capillary pressure gradient-induced backflow. The capillary force drives brine away from the injection outlet toward the evaporation front. Since the evaporation rate of water exceeds the capillary-driven brine backflow rate, water continues to evaporate. When the salt concentration surpasses the solubility limit under the given conditions, excess salt begins to precipitate, and a dry-out front forms. However, its movement is much slower than that of the displacement front. Due to the

hydrophilic nature of sandstone, a thin liquid film persists on pore walls, facilitating the continuous migration of brine and enabling brine absorption over long distances. Additionally, the chosen concentration of brine provides a sufficient reservoir of solute ions, sustaining the salt precipitation process even in the absence of brine replenishment. Ultimately, when the evaporation rate equilibrates with the capillary-driven backflow, the dry-out front stops moving, and localized salt precipitation occurs, resulting in a decrease in permeability. Salt crystals, primarily in the form of polycrystalline aggregates or bulk crystals (Miri et al., 2015) (Figure 2b), accumulate near the injection inlet, causing significant pore blockage.

The formation and accumulation of salt crystals significantly alter wave propagation characteristics. Crystal growth fills pores and pre-existing microcracks, reducing wave path tortuosity, scattering, and energy attenuation at pore boundaries, thereby increasing both P-wave and S-wave velocities. In the DW group, slight velocity fluctuations may be attributed to pressure differentials and water infiltration during displacement. Although dominant flow channels reduce overall pressure gradients, the persistent differential pressures may cause localized structural disturbances. Additionally, deionized water may slightly erode pore surfaces, weakening local structural integrity and causing minor decreases in P-wave velocity (Liu et al., 2024). However, under low differential pressures, such effects are limited and unlikely to significantly influence wave velocities. Conversely, residual water may temporarily fill pores and increase local density, leading to a slight rise in wave velocity. Overall, these fluctuations are small, likely fall within the range of systematic measurement error, and are therefore considered negligible. We also performed X-ray CT imaging to analyze the pore structure near the injection inlet on a layer-by-layer basis. The results indicate a marked reduction in porosity following salt precipitation, consistent with the observed increase in injection pressure, confirming that salt crystallization caused substantial pore blockage.

Short-term increases in wave velocity and apparent densification may occur due to NaCl crystallization in quartz-dominated sandstone, but these phenomena do not necessarily indicate structural strengthening. Small crystals may initially act as pore fillers and marginally stiffen the matrix. However, capillary-driven backflow promotes the continuous accumulation of brine near the injection inlet. As crystal growth progresses within confined pore spaces, crystallization pressures are exerted on pore throats and walls, resulting in localized structural disturbance or even damage. Importantly, these opposing trends are not contradictory. The observed enhancement in wave velocities (both P- and S-waves) reflects a transient pore-filling effect rather than genuine mechanical strengthening, whereas crystallization-induced stresses progressively disturb and damage the rock framework. Consequently, the actual mechanical response and failure characteristics of rocks subjected to salt precipitation require quantitative evaluation and systematic analysis through subsequent mechanical loading tests.

3.2. Mechanical Behavior and Failure Characteristics

Rock failure modes are strongly conditioned by the prevailing stress state. As salt precipitation within pore spaces can markedly increase pore pressure, thereby reducing effective stress and compromising rock-mass stability, this study investigates the mechanical behavior and failure characteristics under such weakened conditions via uniaxial compression testing. Under compressive loading, the resulting failure modes reflect the composite mechanical behavior of the rock and are governed by strength, stiffness, and the spatial distribution of microcracks. The experimental program identified three canonical failure modes under uniaxial compression, namely X-shaped conjugate shear, single-inclined shear, and tensile (splitting) failure, each associated with distinct mechanical responses and failure mechanisms.

Representative samples from the UT, DW, and SP groups were selected to compare mechanical responses and failure modes, and the corresponding stress-strain curves are shown in Figure 3. The uniaxial compression response of the rock before failure can be divided into four stages, namely pore compaction, linear elastic deformation, stable crack propagation, and unstable crack propagation. The UT group exhibits stress-strain curves with a short compaction stage, a well-defined linear elastic segment, relatively high peak strength, and a steep pre-peak slope, displaying single-inclined shear failure. Upon reaching the uniaxial compressive strength (UCS), a through-going macroscopic shear failure typically develops at an angle ranging from 38° to 44° relative to the loading axis, with a relative dispersion of approximately 6%, indicating limited variability among specimens, and failure surfaces commonly showing fragmented particles and powder accumulation. Despite the shear failure, partial interlocking between fragments remains, indicating residual load-bearing capacity. A minority of specimens exhibit mixed shear-tensile failure, likely due to heterogeneity in the initial microcrack distribution within

10.1029/2025GL120303

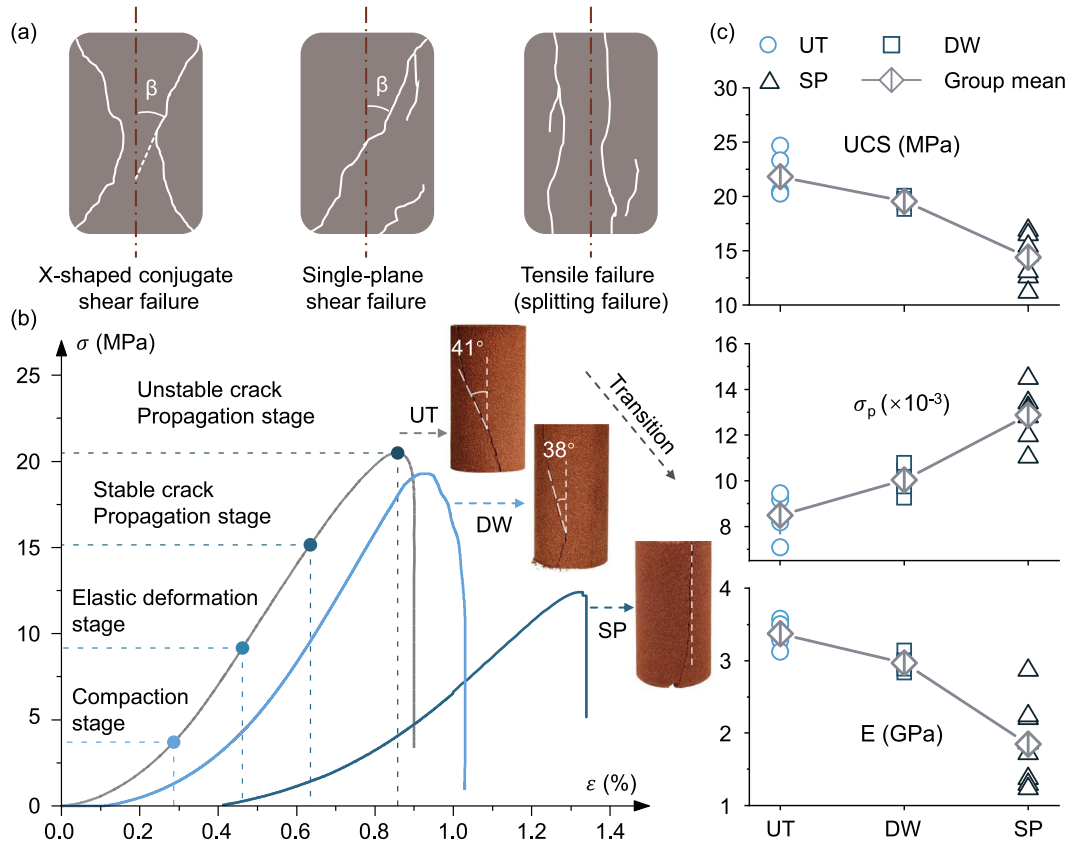

Figure 3. Experimental results showing the mechanical behavior and failure characteristics of the tested samples. (a) Schematic diagram of rock failure modes under uniaxial compression. (b) Representative stress-strain curves and failure modes for each sample group. (c) Mechanical parameters (uniaxial compressive strength, σ_p, and E) with their averages and trends.

the rock matrix. Near the specimen ends, cracks tend to propagate parallel to the loading axis, reflecting localized stress perturbations caused by boundary constraints, a typical end effect. In the DW group, microstructural disturbances may have arisen from deionized-water saturation followed by $scCO_2$ displacement, yet the overall stress-strain behavior and failure mode are similar to the UT group, with shear failure still dominant. The elastic phase appears slightly shortened and crack initiation occurs marginally earlier, suggesting a modest reduction in local stiffness while overall structural integrity remains largely intact.

In contrast, SP specimens affected by salt precipitation exhibit distinct mechanical responses and failure modes. Their stress-strain curves shift downward and to the right, indicating reduced peak strength and increased peak strain. The pre-peak slope diminishes markedly, and the compaction phase extends over a larger strain interval. Together, these features imply a higher proportion of compressible constituents, such as microcracks and loosely bonded salt crystals, which necessitate prolonged compaction before the elastic regime and yield a lower initial stiffness. The failure morphology is consistent with these mechanical signatures. Upon reaching the UCS, most SP specimens develop a dominant axial tensile failure, indicating a transition from shear-to tensile-dominated failure. In some cases, a combined failure mode is observed in which the primary axial failure is accompanied by a secondary oblique failure, and fragment spalling frequently occurs near crack tips. This sequence-extended compaction, reduced mechanical competence, and tensile failure dominance-reflects stress redistribution driven by pore-scale weakening and culminates in further degradation of structural stability.

Across treatments, mechanical parameters degrade systematically from UT to DW to SP, with detailed mechanical data shown in Table 1. Compared with the UT group, DW specimens show a slight reduction in UCS and elastic modulus, along with a small increase in peak strain, indicating minor stiffness loss while overall structural integrity is largely preserved. In contrast, SP specimens exhibit pronounced weakening. The average UCS

Table 1
Petrophysical Properties and Mechanical Parameters Derived From Stress-Strain Curves for Used Samples

Sample	Porosity (%)	Permeability (mD)	σ_p (MPa)	ε_p (10^{-3})	E (GPa)
UT-1	23.95	671.12	20.489	8.542	3.280
UT-2	23.29	701.54	20.296	8.184	3.581
UT-3	23.74	713.62	24.67	9.185	3.367
UT-4	23.55	645.86	20.263	7.905	3.507
UT-5	24.07	756.23	23.307	9.455	3.125
DW-1	23.12	692.52	19.746	9.255	3.002
DW-2	23.68	620.14	18.823	10.466	3.141
DW-3	23.97	667.59	20.057	9.953	2.965
DW-4	23.45	782.32	19.442	9.756	2.886
DW-5	23.6	680.57	19.729	10.785	2.874
SP-1	23.74	714.16	12.582	13.205	1.371
SP-2	24.01	772.01	11.171	13.421	1.290
SP-3	23.94	786.23	16.878	11.968	2.199
SP-4	23.46	668.00	15.050	13.121	2.127
SP-5	23.52	697.46	16.453	12.988	2.236
SP-6	24.08	803.48	13.058	12.791	2.364
SP-7	23.63	756.35	15.404	11.043	1.865
SP-8	23.41	724.88	14.543	14.481	1.713

decreases from 21.805 to 14.392 MPa (a 34.00% reduction), accompanied by an approximately 51.64% increase in the corresponding peak strain. The elastic modulus decreases from an average of 3.371–1.846 GPa, corresponding to an average reduction of about 45.25%. These shifts align with a transition in failure mode from shear-dominated (UT/DW) to tensile-dominated behavior in SP, often with compound cracking and spalling. Mechanistically, salt precipitation introduces compressible features and weakly bonded NaCl-quartz interfaces that produce elastic modulus mismatches and discontinuous stress-transmission paths. These heterogeneities concentrate stress, promote preferential crack growth and propagation, and direct crack development toward an axial-splitting path, thereby lowering stiffness and strength despite any localized densification or wave velocity increases. Consequently, salt-induced microstructural damage governs the observed transition of the rock failure mode from shear-dominated to tensile-dominated behavior.

3.3. Microstructural Analysis of the Salt-Crystallization-Induced Failure Transition

Analysis of the macroscopic response shows that salt-crystal nucleation and growth markedly degrade rock mechanical properties and result in a transition in failure mode from shear-to tensile-dominated. To elucidate the microscopic origins of this transition, we employ multiscale microscopic characterization to interrogate internal structure and damage, focusing on how salt-induced local stress fields at the grain scale govern crack initiation, propagation, and ultimately macroscopic failure behavior.

To capture failure morphology, we reconstructed 3D geometries of failed specimens using CT. Figure 4 shows untreated samples with through-going shear failures inclined to the loading axis (consistent with 2D views), though some may be underestimated due to post-failure contact that suppresses openings. By contrast, SP specimens exhibit dominant axial (tensile) failures with secondary cracks, confirming a shift from shear-to tensile-dominated behavior. Failures were extracted with identical segmentation parameters and thresholds to ensure comparability. The fracture volume fraction within the failure zone was calculated to quantify crack development. Shear-failed specimens cluster near 1.3% with oscillating dispersion. SP specimens average 1.2% and display larger spatial variability, indicating more heterogeneous, tension-driven multi-crack systems.

At the pore scale, microstructural damage arises from crystallization pressure generated during salt growth under CO_2 displacement. Supersaturation, pore geometry, and interfacial forces (e.g., disjoining pressure) govern the

10.1029/2025GL120303

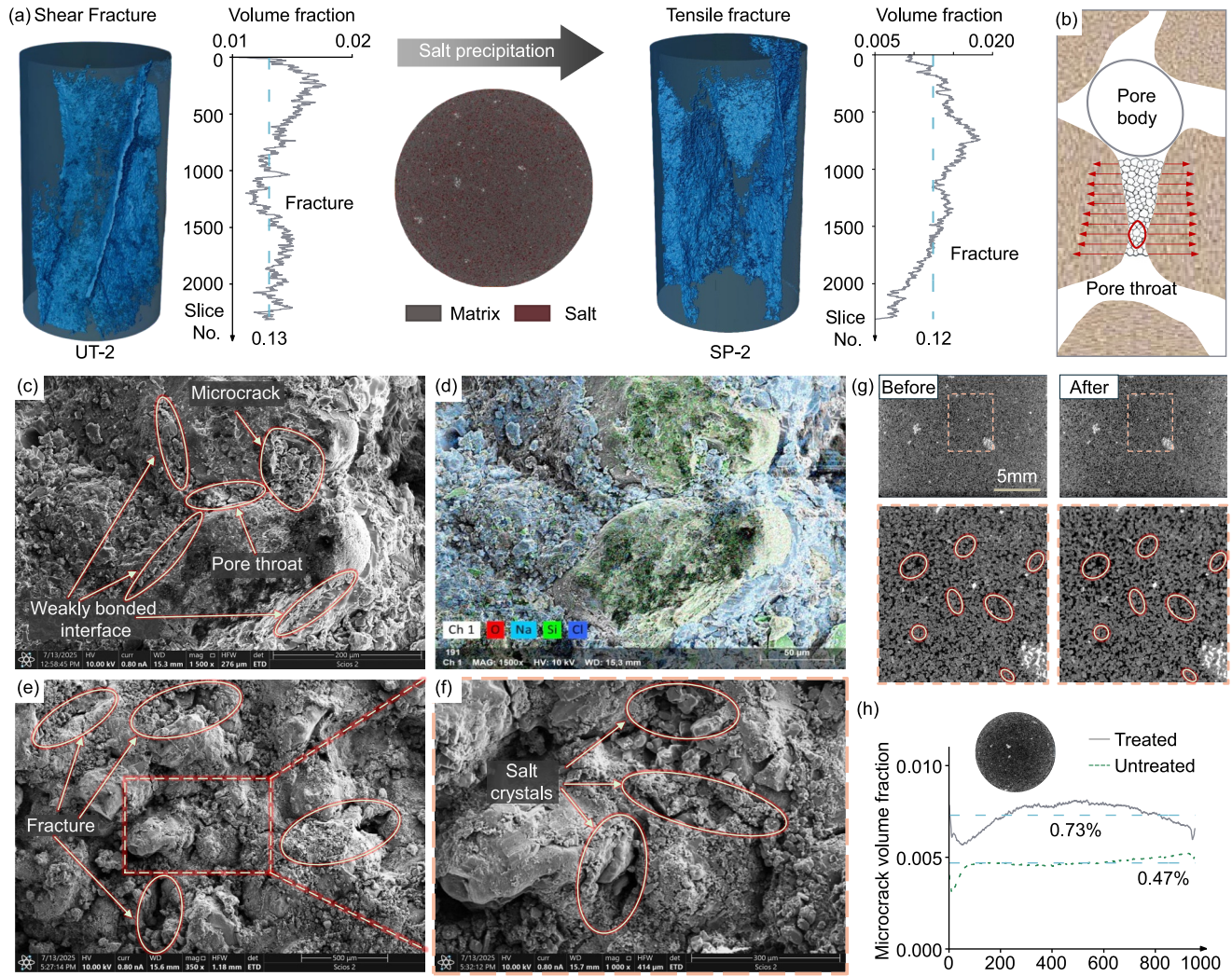

Figure 4. Microstructural analysis showing salt-crystallization-induced evolution of the internal pore structure in the samples. (a) CT-based 3D reconstructed failure modes of representative samples from the UT and SP groups with corresponding fracture volume fractions. (b) Schematic illustration of stress acting on pore throats during salt crystallization. (c)–(f) scanning electron microscopy coupled with energy-dispersive spectroscopy images showing intergranular failure along weak bonding interfaces and crystallization-induced microcrack propagation at pore throats. (g) CT slices along the sample axis before and after salt crystallization (top, scale bar = 5 mm) and corresponding 4 × magnified views of selected regions (bottom), together illustrating microcrack propagation. (h) CT-based analysis showing increased microcrack volume fraction after salt crystallization.

collapse of thin brine films and crystal-wall contact. Porous and water-wet salt crystals formed at gas-liquid interfaces sustain capillary backflow, fueling continued growth. Once crystallization pressure exceeds the threshold disjoining pressure, crystals load the walls. The tensile strength of sandstone typically ranges from 0.9 to 1.1 MPa (Vogler et al., 2017). In contrast, the crystallization pressure generated by NaCl crystallization in confined spaces is approximately 200 ± 55 MPa (Desarnaud et al., 2016), sufficient to exceed the tensile strength of sandstone and cause pore rupture, which links isolated voids, widens pre-existing cracks, and reorients them along tensile paths. CT image processing with a top-hat filter and uniform threshold shows microcrack volume rising from 0.47% in UT to 0.73% in SP. This increase indicates enhanced initiation and propagation of microcracks. Under external loading, these flaws concentrate stress. Wing cracks initiate along the axial maximum principal stress and then coalesce to produce macroscale tensile failure. SP shows more extensive coalescence than UT, linking pore-scale processes to the observed mode transition.

Under SEM-EDS, salt crystals are embedded within pores without strong bonding to the quartz matrix, creating weak interfaces that localize stress and foster crack initiation. Partially connected crystal aggregates in pore throats suggest crystallization-induced microcracks between adjacent pores, facilitating tensile cracking.

Pronounced crack propagation within the matrix indicates reactivation of defects by crystallization pressure. EDS shows no significant geochemical alteration, implying a predominantly physical mechanism. Higher-magnification imaging of fracture-rich regions shows salt concentrated within fracture networks, consistent with crystallization pressure driving opening and connectivity. The quartz framework remains largely intact, with damage concentrated along grain boundaries (intergranular failure) and cracks exhibiting tensile morphologies. Collectively, these microstructural observations account for the macroscopic transition from shear-dominated failure in UT or DW to tensile-dominated behavior in SP.

4. Conclusion

This study shows that salt precipitation substantially modifies the mechanical behavior of reservoir rocks relevant to GCS. Salt crystallization occurs within pore spaces, occludes pore throats, and densifies the microstructure, thereby increasing elastic wave velocity. At the specimen scale, however, it degrades mechanical performance by reducing both strength and stiffness. Critically, 2D observations and 3D CT reconstructions reveal a transition in failure mode from shear-dominated (UT and DW) to tensile-dominated (SP). Microscale analyses indicate that salt primarily occupies pores without forming strong bonding with the quartz framework, establishing stress concentration zones. Crystallization pressure further damages the matrix, links previously isolated micropores, and drives microcrack nucleation and propagation. As a result, salt precipitation increases the microcrack volume fraction and compromises structural integrity, even when final fracture volumes are comparable across groups. SEM imaging shows that post-precipitation failure is characterized by intergranular cracking, consistent with a weak-bonding mechanism. Overall, the findings delineate a coupled pathway connecting salt precipitation to mechanical degradation and microstructural evolution, providing experimental evidence and mechanistic insights into near-wellbore alterations during GCS. The results also offer a solid rock-mechanical basis to support the investigation and evaluation of microseismic triggering mechanisms.

Conflict of Interest

The authors declare no conflicts of interest relevant to this study.

Data Availability Statement

The data underlying this article are available in Ju and An (2025).

Acknowledgments
This work was supported by the National Science and Technology Major Project (2024ZD1003903), National Natural Science Foundation of China (52474105, 52304098), Shenzhen Science and Technology Program (JCYJ20220818095605012), and Research Team Cultivation Program of Shenzhen University (2023QNT004).

References

Alam, M. M., Hjuler, M. L., Christensen, H. F., & Fabricius, I. L. (2014). Petrophysical and rock-mechanics effects of CO_2 injection for enhanced oil recovery: Experimental study on chalk from South Arne field, North Sea. *Journal of Petroleum Science and Engineering*, *122*, 468–487. https://doi.org/10.1016/j.petrol.2014.08.008

An, S., Erfani, H., Hellevang, H., & Niasar, V. (2021). Lattice-Boltzmann simulation of dissolution of carbonate rock during CO_2-saturated brine injection. *Chemical Engineering Journal*, *408*, 127235. https://doi.org/10.1016/j.cej.2020.127235

An, S., Hasan, S., Erfani, H., Babaei, M., & Niasar, V. (2020). Unravelling effects of the pore-size correlation length on the two-phase flow and solute transport properties: GPU-based pore-network modeling. *Water Resources Research*, *56*(8), e2020WR027403. https://doi.org/10.1029/2020wr027403

Baumann, G., Henninges, J., & De Lucia, M. (2014). Monitoring of saturation changes and salt precipitation during CO_2 injection using pulsed neutron-gamma logging at the Ketzin pilot site. *International Journal of Greenhouse Gas Control*, *28*, 134–146. https://doi.org/10.1016/j.ijggc.2014.06.023

Bergstad, M., & Shokri, N. (2016). Evaporation of NaCl solution from porous media with mixed wettability. *Geophysical Research Letters*, *43*(9), 4426–4432. https://doi.org/10.1002/2016gl068665

Celia, M. A., Bachu, S., Nordbotten, J. M., & Bandilla, K. W. (2015). Status of CO_2 storage in deep saline aquifers with emphasis on modeling approaches and practical simulations. *Water Resources Research*, *51*(9), 6846–6892. https://doi.org/10.1002/2015wr017609

Chai, R., Liu, Y., Wang, J., Liu, Q., & Rui, Z. (2022). CO_2 utilization and sequestration in Reservoir: Effects and mechanisms of CO_2 electrochemical reduction. *Applied Energy*, *323*, 119584. https://doi.org/10.1016/j.apenergy.2022.119584

Chai, R., Liu, Y., Xue, L., Rui, Z., Zhao, R., & Wang, J. (2022). Formation damage of sandstone geothermal reservoirs: During decreased salinity water injection. *Applied Energy*, *322*, 119465. https://doi.org/10.1016/j.apenergy.2022.119465

Chen, X.-S., Hu, R., Zhou, C.-X., Xiao, Y., Yang, Z., & Chen, Y.-F. (2024). Capillary-driven backflow during salt precipitation in a rough fracture. *Water Resources Research*, *60*(3), e2023WR035451. https://doi.org/10.1029/2023wr035451

Desarnaud, J., Bonn, D., & Shahidzadeh, N. (2016). The pressure induced by salt crystallization in confinement. *Scientific Reports*, *6*(1), 30856. https://doi.org/10.1038/srep30856

De Silva, G., Ranjith, P. G., & Perera, M. (2015). Geochemical aspects of CO_2 sequestration in deep saline aquifers: A review. *Fuel*, *155*, 128–143. https://doi.org/10.1016/j.fuel.2015.03.045

Eberli, G. P., Baechle, G. T., Anselmetti, F. S., & Incze, M. L. (2003). Factors controlling elastic properties in carbonate sediments and rocks. *The Leading Edge*, *22*(7), 654–660. https://doi.org/10.1190/1.1599691

Espinosa-Marzal, R. M., & Scherer, G. W. (2010). Advances in understanding damage by salt crystallization. *Accounts of Chemical Research*, *43*(6), 897–905. https://doi.org/10.1021/ar9002224

Eyitayo, S. I., Watson, M. C., Ispas, I., & Kolawole, O. (2025). Geochemical interactions of supercritical CO_2-brine-rock under varying injection strategies: Implications for mechanical integrity in aquifers. *Rock Mechanics and Rock Engineering*, *58*(7), 7181–7202. https://doi.org/10.1007/s00603-025-04496-7

Gandomkar, A., Torabi, F., Nasriani, H. R., & Enick, R. M. (2025). Maximising CO_2 sequestration efficiency in deep saline aquifers through in-situ generation of CO_2-in-brine foam incorporating novel CO_2-soluble non-ionic surfactants. *Chemical Engineering Journal*, *521*, 166102. https://doi.org/10.1016/j.cej.2025.166102

Grude, S., Landrø, M., & Dvorkin, J. (2014). Pressure effects caused by CO_2 injection in the Tubåen Fm., the Snøhvit field. *International Journal of Greenhouse Gas Control*, *27*, 178–187. https://doi.org/10.1016/j.ijggc.2014.05.013

Hangx, S., van der Linden, A., Marcelis, F., & Bauer, A. (2013). The effect of CO_2 on the mechanical properties of the captain sandstone: Geological storage of CO_2 at the Goldeneye field (UK). *International Journal of Greenhouse Gas Control*, *19*, 609–619. https://doi.org/10.1016/j.ijggc.2012.12.016

Hassani, A., Smith, P., & Shokri, N. (2024). Negative correlation between soil salinity and soil organic carbon variability. *Proceedings of the National Academy of Sciences*, *121*(18), e2317332121. https://doi.org/10.1073/pnas.2317332121

Jannesarahmadi, S., Aminzadeh, M., Helmig, R., Or, D., & Shokri, N. (2024). Quantifying salt crystallization impact on evaporation dynamics from porous surfaces. *Geophysical Research Letters*, *51*(22), e2024GL111080. https://doi.org/10.1029/2024gl111080

Ji, T., Haghi, A. H., Jiang, P., Chalaturnyk, R., & Xu, R. (2025). Capillary-driven transport and precipitation of salt in heterogeneous structures during carbon sequestration. *Geophysical Research Letters*, *52*(13), e2024GL114388. https://doi.org/10.1029/2024gl114388

Ju, J., & An, S. (2025). Salt precipitation-driven rock failure mode transition during CO_2 geological sequestration. *Mendeley Data*. https://doi.org/10.17632/jcf3xsjf4c.1

Kivi, I. R., Boyet, A., Wu, H., Walter, L., Hanson-Hedgecock, S., Parisio, F., & Vilarrasa, V. (2023). Global physics-based database of injection-induced seismicity. *Earth System Science Data*, *15*(7), 3163–3182. https://doi.org/10.5194/essd-15-3163-2023

Kivi, I. R., De Simone, S., & Krevor, S. (2025). A simplified physics model for estimating subsurface CO_2 storage resources constrained by fault slip potential. *Journal of Rock Mechanics and Geotechnical Engineering*. https://doi.org/10.1016/j.jrmge.2025.06.031

Krevor, S., De Coninck, H., Gasda, S. E., Ghaleigh, N. S., de Gooyert, V., Hajibeygi, H., et al. (2023). Subsurface carbon dioxide and hydrogen storage for a sustainable energy future. *Nature Reviews Earth and Environment*, *4*(2), 102–118. https://doi.org/10.1038/s43017-022-00376-8

Li, S., Wang, P., Wang, Z., Cheng, H., & Zhang, K. (2023). Strategy to enhance geological CO_2 storage capacity in saline aquifer. *Geophysical Research Letters*, *50*(3), e2022GL101431. https://doi.org/10.1029/2022gl101431

Li, S., Zhang, S., Xing, H., & Zou, Y. (2022). CO_2-brine-rock interactions altering the mineralogical, physical, and mechanical properties of carbonate-rich shale oil reservoirs. *Energy*, *256*, 124608. https://doi.org/10.1016/j.energy.2022.124608

Liu, X., Chen, J., Liu, B., Wang, S., Liu, Q., & Luo, J. (2024). Effects of seepage pressure on the mechanical behaviors and microstructure of sandstone. *Journal of Rock Mechanics and Geotechnical Engineering*, *16*(6), 2033–2051. https://doi.org/10.1016/j.jrmge.2023.09.010

Lyu, Q., Deng, J., Tan, J., Ding, Y., Shi, Y., Feng, G., & Shen, Y. (2024). Effects of CO_2-saturated brine imbibition on the mechanical and seepage characteristics of Longmaxi shale. *Energy*, *308*, 132889. https://doi.org/10.1016/j.energy.2024.132889

Miri, R., van Noort, R., Aagaard, P., & Hellevang, H. (2015). New insights on the physics of salt precipitation during injection of CO_2 into saline aquifers. *International Journal of Greenhouse Gas Control*, *43*, 10–21. https://doi.org/10.1016/j.ijggc.2015.10.004

Pellet, F. L., & Fabre, G. (2007). Damage evaluation with p-wave velocity measurements during uniaxial compression tests on argillaceous rocks. *International Journal of Geomechanics*, *7*(6), 431–436. https://doi.org/10.1061/(asce)1532-3641(2007)7:6(431)

Scherer, G. W. (2004). Stress from crystallization of salt. *Cement and Concrete Research*, *34*(9), 1613–1624. https://doi.org/10.1016/j.cemconres.2003.12.034

Shokri, N., Hassani, A., & Sahimi, M. (2024). Multi-scale soil salinization dynamics from global to pore scale: A review. *Reviews of Geophysics*, *62*(4), e2023RG000804. https://doi.org/10.1029/2023rg000804

Song, Y., Jun, S., Na, Y., Kim, K., Jang, Y., & Wang, J. (2023). Geomechanical challenges during geological CO_2 storage: A review. *Chemical Engineering Journal*, *456*, 140968. https://doi.org/10.1016/j.cej.2022.140968

Sun, X., Liu, K., An, S., Hellevang, H., Cao, Y., Alcalde, J., et al. (2025). A review of experimental investigations on salt precipitation during CO_2 geological storage. *Geoenergy Science and Engineering*, *244*, 213451. https://doi.org/10.1016/j.geoen.2024.213451

Sun, Y., Li, Q., Yang, D., & Liu, X. (2016). Laboratory core flooding experimental systems for CO_2 geosequestration: An updated review over the past decade. *Journal of Rock Mechanics and Geotechnical Engineering*, *8*(1), 113–126. https://doi.org/10.1016/j.jrmge.2015.12.001

Tao, J., Meng, S., Li, D., Rui, Z., Liu, H., & Xu, J. (2023). Analysis of CO_2 effects on porosity and permeability of shale reservoirs under different water content conditions. *Geoenergy Science and Engineering*, *226*, 211774. https://doi.org/10.1016/j.geoen.2023.211774

Vialle, S., & Vanorio, T. (2011). Laboratory measurements of elastic properties of carbonate rocks during injection of reactive CO_2-saturated water. *Geophysical Research Letters*, *38*(1), L01302. https://doi.org/10.1029/2010gl045606

Vilarrasa, V., Carrera, J., Olivella, S., Rutqvist, J., & Laloui, L. (2019). Induced seismicity in geologic carbon storage. *Solid Earth*, *10*(3), 871–892. https://doi.org/10.5194/se-10-871-2019

Viswanathan, H. S., Ajo-Franklin, J., Birkholzer, J. T., Carey, J. W., Guglielmi, Y., Hyman, J., et al. (2022). From fluid flow to coupled processes in fractured rock: Recent advances and new frontiers. *Reviews of Geophysics*, *60*(1), e2021RG000744. https://doi.org/10.1029/2021rg000744

Vogler, D., Walsh, S. D., Dombrovski, E., & Perras, M. A. (2017). A comparison of tensile failure in 3d-printed and natural sandstone. *Engineering Geology*, *226*, 221–235. https://doi.org/10.1016/j.enggeo.2017.06.011

Wang, B., Chang, Y., Ma, R., Wang, X., Wang, H., & Zeng, F. (2025). Insights from dynamics, mechanisms, factors and mitigation strategies of salt precipitation for CO_2 geo-storage within saline aquifer. *Earth-Science Reviews*, *267*, 105170. https://doi.org/10.1016/j.earscirev.2025.105170

Wang, W., Xie, Q., An, S., Bakhshian, S., Kang, Q., Wang, H., et al. (2023). Pore-scale simulation of multiphase flow and reactive transport processes involved in geologic carbon sequestration. *Earth-Science Reviews*, *247*, 104602. https://doi.org/10.1016/j.earscirev.2023.104602

Xie, S., Shao, J., & Xu, W. (2011). Influences of chemical degradation on mechanical behaviour of a limestone. *International Journal of Rock Mechanics and Mining Sciences*, *48*(5), 741–747. https://doi.org/10.1016/j.ijrmms.2011.04.015

Yan, L., Niftaliyev, R., Voskov, D., & Farajzadeh, R. (2025). Dynamics of salt precipitation at pore scale during CO_2 subsurface storage in saline aquifer. *Journal of Colloid and Interface Science*, *678*, 419–430. https://doi.org/10.1016/j.jcis.2024.08.265

Yu, P., Dempsey, D., Rinaldi, A. P., Calibugan, A., Ritz, V. A., & Archer, R. (2023). Association between injection and microseismicity in geothermal fields with multiple wells: Data-driven modeling of Rotokawa, New Zealand, and Húsmúli, Iceland. *Journal of Geophysical Research: Solid Earth*, *128*(4), e2022JB025952. https://doi.org/10.1029/2022jb025952

Zhou, D., Zhao, Z., Liao, J., & Sun, Z. (2011). A preliminary assessment on CO_2 storage capacity in the Pearl River Mouth Basin offshore Guangdong. *China, International Journal of Greenhouse Gas Control*, *5*(2), 308–317. https://doi.org/10.1016/j.ijggc.2010.09.011